Journal of Nuclear Materials 452 (2014) 614–627

Contents lists available at ScienceDirect

Journal of Nuclear Materials

journal homepage: www.elsevier.com/locate/jnucmat

Presented at the NuMat 2012 Conference, 22–25 October 2012, Osaka, Japan

Microbeam X-ray Absorption Near-Edge Spectroscopy study of the oxidation of Fe and Nb in zirconium alloy oxide layers

Adrien Couet [a,*], Arthur T. Motta [a], Benoit de Gabory [a], Zhonghou Cai [b]

[a] Department of Mechanical and Nuclear Engineering, Penn State University, University Park, PA 16802, USA
[b] Advanced Photon Source, XFD 401 B3194, Argonne National Laboratory, 9700 South Cass Ave., Argonne, IL 60439, USA

ARTICLE INFO

Article history:
Received 3 June 2013
Accepted 20 May 2014
Available online 29 May 2014

ABSTRACT

Alloy optimization of zirconium based alloys used for nuclear fuel cladding is key to increasing corrosion resistance and reducing hydrogen pickup. The mechanism by which alloying elements influence these processes is investigated by focusing on the chemical state evolution of two alloying elements, Fe and Nb, when incorporated into the growing oxide layers of various production zirconium alloys – Zircaloy-4, ZIRLO® and Zr–2.5Nb – as well as a model alloy – Zr–0.4Fe–0.2Cr. X-ray Absorption Near-Edge Spectroscopy (XANES) measurements to determine the evolution of their oxidation states is performed using micro-beam synchrotron radiation on cross sectional oxide samples. A thin (~12 μm) cross-sectional sample of Zircaloy-4 oxide was also designed and fabricated to differentiate the signal coming from the Fe in solid solution from the signal coming from the Fe in precipitates. The XANES spectra were fitted using a combination of standards, to determine the evolution of the oxidized fractions of Fe and Nb in the oxide as function of distance from the oxide/metal interface. The results show that the oxidation of Fe and Nb in the oxide layer is delayed relative to that of Zr. Both the second phase precipitates and solid solution Fe atoms were initially incorporated in metallic form into the oxide layer, although it appears that Fe in solid solution oxidizes first. It is shown that after a given distance from the metal/oxide interface (which is alloy dependent), the alloying elements start to oxidize. Qualitative TEM examinations of precipitates embedded in zirconium oxide layers correlate well with the quantitative XANES results. These results allow a discussion of a qualitative oxidation model of Fe and Nb in Zr alloys.

1. Introduction

With increased burnups and longer lifetimes in nuclear reactors, uniform corrosion of zirconium alloy nuclear fuel cladding and the associated hydrogen pickup can become life limiting in existing and advanced light water reactors, due to the associated ingress of hydrogen and precipitation of hydrides, which can cause cladding embrittlement [1,2]. It has been pointed out that several factors can control the uniform corrosion of zirconium alloys [3]. Alloy optimization of zirconium based alloys used for nuclear fuel cladding is a key to increasing corrosion resistance and reducing hydrogen pickup. However, a complete mechanistic understanding of the role of alloying elements in the corrosion and hydrogen pickup processes is still lacking.

Because very small alloying element differences cause large differences in corrosion and hydrogen pickup, it is natural to examine the behavior of alloying elements in the oxide layer for clues to the origin of the differences between alloys. In this study, we focus on the evolution of the chemical states of two alloying elements, Fe and Nb, when incorporated into the zirconium alloy oxide layers formed during autoclave testing of various zirconium alloys oxidized in pure water. The solubility of Fe in the alloys is less than a few hundreds of wt ppm [4], so that Fe is mainly found in $Zr(Cr,Fe)_2$ intermetallic precipitates in Zircaloy-4 (Zr–1.45Sn–0.2Fe–0.1Cr) and in ZrNbFe precipitates in ZIRLO®[1] (Zr–1.0Sn–1.0Nb–0.1Fe) [5–7]. In ZIRLO and in Zr–2.5Nb alloys, Nb is found both in solid solution (the Nb solubility limit is approximately 0.5 wt% in the α zirconium phase) and in βNb and $Zr(Nb,Fe)_2$ precipitates [8]. The size, chemical composition and distribution of these precipitates (and so their equilibrium with Nb and Fe concentrations in solid solution) may have a profound impact on the corrosion resistance and the hydrogen pickup of Zircaloy-4 and Zr–Nb based alloys [9–14]. However, despite extensive research, the specific influence of the alloying elements in precipitates and in solid solution on the

* Corresponding author. Tel.: +1 814 865 9709.
E-mail address: adrien.couet@gmail.com (A. Couet).

[1] ZIRLO® is a registered trademark of Westinghouse Electric Company LLC in the United States and may be registered in other countries throughout the world. All rights reserved. Unauthorized use is strictly prohibited.

http://dx.doi.org/10.1016/j.jnucmat.2014.05.047
0022-3115/

mechanisms of corrosion and its associated hydrogen pickup is not well understood [11–13,15].

Given the relative free energies of oxidation, we expect Nb and Fe to oxidize at a higher oxygen potential compared to zirconium [16]. Delayed oxidation of Fe and Nb in second phase precipitates compared to the zirconium phase has been previously reported from transmission electron microscopy (TEM) examinations [17,18]. However, the precise evolution of the chemical state of Fe and Nb, both in second phase precipitates and in solid solution, upon their incorporation into the zirconium alloy oxide layers is still unknown, especially its variations with distance from the oxide/metal interface.

In this work, a microbeam X-ray Absorption Near-Edge Spectroscopy (μXANES) investigation of the evolution of Fe and Nb oxidation states when incorporated into oxide layers formed on various alloys (Zircaloy-4, ZIRLO, Zr–2.5Nb and Zr–0.4Fe–0.2Cr) is performed on cross-sectional oxide samples using micro-beam synchrotron radiation. Previous XANES studies of the evolution of Fe and Nb oxidation in pre-transition zirconium alloys using synchrotron radiation have focused on either flakes of powdered oxide layer, thus determining only the average element oxidation state [19], or, when some oxide depth resolution was made possible using surface sensitive XANES on sputtered oxide layers, the XANES signal originated from the contributions of both the element in precipitates and the element in solid solution [20,21]. Other XANES studies of Nb oxidation in various Zr–Nb alloys have also been reported but in those studied the sample geometry did not allow precise oxide depth resolution [22].

In this study, Fe and Nb oxidation states were determined as function of oxide depth on multiple pre- and post-transitions archived samples of Zircaloy-4, ZIRLO, Zr–2.5Nb and Zr–0.4Fe–0.2Cr. Also, in the case of Fe in Zircaloy-4, a new sample preparation technique has allowed us to perform studies on samples prepared by Focused Ion Beam (FIB) to deconvolute the signals from precipitates and solid solution. Thus, it was also possible to separate the chemical state evolution of Fe in ZrO_2 solid solution from that of Fe in $Zr(Cr,Fe)_2$ intermetallic precipitates embedded in the oxide layer. After reporting experimental results, the oxidation process is discussed and an oxidation model of alloying elements in zirconium alloys is proposed.

2. Experimental procedures

2.1. XANES experiment

The XANES experiments were performed at the 2ID-D beamline of the Advanced Photon Source (APS) at Argonne National Laboratory. Using zone plate diffraction gratings, the X-ray microprobe in the experimental station produces a monochromatic X-ray beam of size 0.2 μm × 0.2 μm (FWHM) with a photon flux of 5×10^9 photons/s within an X-ray energy bandwidth (dE/E) of 0.01%. Fig. 1 shows a schematic of the scattering and data acquisition geometry for the XANES experiments: the microbeam is placed in frontal incidence on the region of interest of the specimen to keep the probed surface area as small as possible. The XANES signals are recorded in fluorescence, with a fluorescence detector placed at approximately 85° from the incident beam to avoid elastic scattering perturbation of the fluorescence signal. The XANES scan energy step is 0.5 eV and the chosen energy windows are 100 eV (from 7.09 keV to 7.19 keV) for Fe (the Fe K-edge is located at 7.12 keV), and 140 eV (from 18.94 keV to 19.08 keV) for Nb (the Nb K-edge is located at 18.98 keV). In the case of the thin cross-sectional sample prepared by focused ion beam (FIB), an ionization chamber was placed at the end of the beamline to detect the transmission signal. The transmitted signal was only used to determine the thin sample thickness. No XANES in transmission have been performed because the Fe K-edge in transmission was not detectable, probably due to the overall low concentration of Fe in the microbeam path. All the measurements were performed at room temperature.

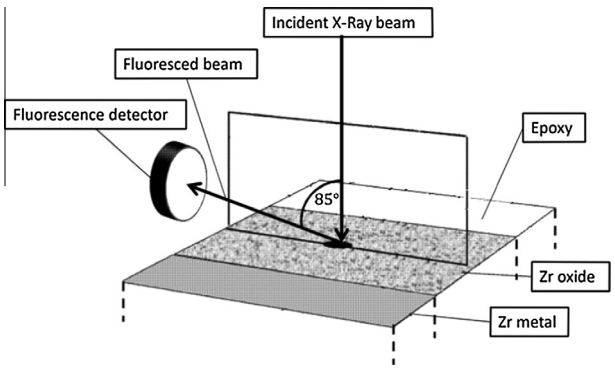

Fig. 1. Schematic drawing of the geometry of data acquisition at the synchrotron beamline.

The experimental procedure consisted of first taking a fluorescence scan of the Zr L-edge (in case of XANES on Fe) or Zr K-edge (in case of XANES on Nb), in order to determine the position of the oxide/metal and oxide/water interfaces. Then XANES scans were performed at various distances of the interface, in the oxide and in the metal. The XANES experiment was then conducted by setting the beam at a particular oxide location and varying the energy in small increments within an energy window containing the edge of the element of interest. This was repeated for the entire oxide layer. After each XANES scan, the current beam position was confirmed by running an extra fluorescence scan to rule out specimen drift during the experiment.

2.2. Corrosion testing and samples preparation

Corrosion tests were performed by Westinghouse Electric Co. in their laboratory facility in Churchill, PA. Zircaloy-4, ZIRLO and Zr–2.5Nb samples were corroded in the form of tube and sheet corrosion coupons [23]. The Zircaloy-4 composition is Zr–1.45Sn–0.2Fe–0.1Cr (the alloying contents are indicated in weight percent). The composition of ZIRLO is Zr–1.0Sn–1.0Nb–0.1Fe, while the Zr–2.5Nb alloy contains an impurity level of Fe varying from 100 wt ppm to 600 wt ppm. A model alloy of composition Zr–0.4Fe–0.2Cr in the form of a corrosion sheet coupon (25 mm × 20 mm × 0.8 mm) with an average precipitate diameter of 110 nm has also been investigated. The processing of these alloys is described elsewhere [23].

The samples were corroded in 360 °C pure water at saturation pressure of 2708.6 psi (18.7 MPa) according to ASTM G2 [24]. A list of the samples investigated in this work is shown in Table 1 and their weight gain as a function of exposure time is plotted in Fig. 2. The arrows in Fig. 2 represent the samples that have been archived and used in the microbeam XANES experiments. The exact exposure time and oxide thickness (determined from weight gains, 1 μm = 14.77 mg/dm^2) for these samples are indicated in Table 1. Visual examination and cross sectional SEM images have shown that the oxide layers were adherent and no spallation occurred during corrosion of any of these samples.

2.2.1. Thick sample preparation

All samples were prepared as thick cross-sectional samples, in the form of small transverse cross-sections (the transverse direction being normal to the cross section) of corroded tube coupons according to the following procedure. A thin segment (2 mm × 15 mm × 0.8 mm) was cut from the corrosion coupon

Table 1
List of the samples used for the XANES experiments. Their exposure time (in days) and their oxide thickness (in microns, derived from the weight gain) are indicated.

			Exposure time (days)	Oxide thickness (μm)
Fe	Zircaloy-4	Before 1st transition	45	1.7
			60	1.8
		Between 1st and 2nd transitions	90	2.8
			105	3.4
			120	3.6
			135	3.9
			150	4.1
			165	4.2
		Between 2nd and 3rd transitions	225	5.9
			255	6.4
	Zr–0.4Fe–0.2Cr	Pre-breakaway	173	2.4
			463	3.2
	ZIRLO	Before 1st transition	30	1.7
			60	2.3
			90	2.7
Nb	ZIRLO	Before 1st transition	30	1.7
			60	2.3
			90	2.7
		Between 1st and 2nd transitions	240	5.5
	Zr–2.5Nb	Before 1st transition	60	2.2
			120	2.9
			150	3.2

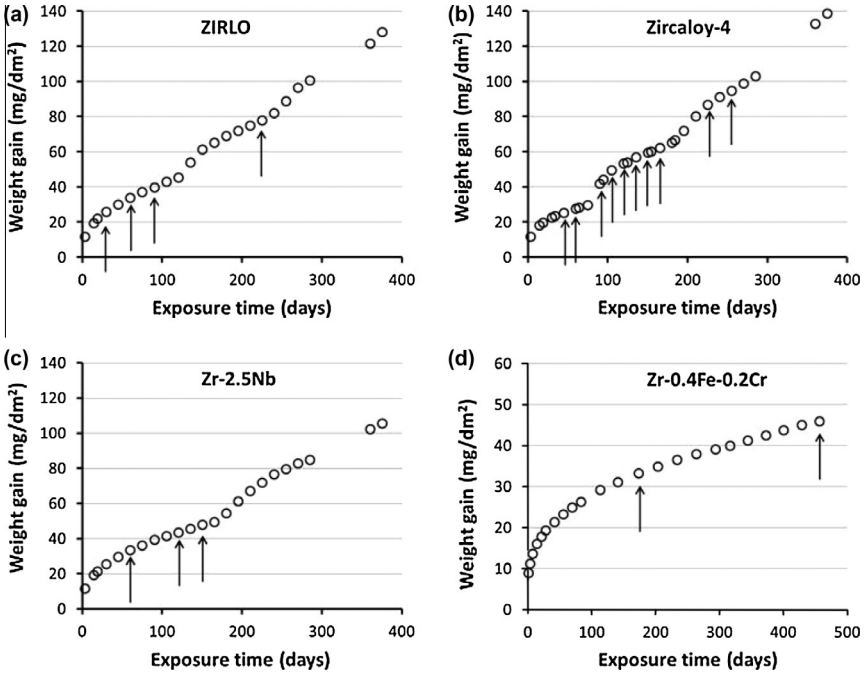

Fig. 2. Weight gain (in mg/dm^2) as a function of exposure time for the following alloys: (a) ZIRLO tube, (b) Zircaloy-4 sheet, (c) Zr–2.5Nb, (d) Zr–0.4Fe–0.2Cr. The arrows indicate the samples that have been archived and studied for XANES, and which are listed in Table 1.

using a low-speed diamond saw to expose its cross-section and then ground to a thickness of about 0.25 mm on one side to facilitate subsequent mounting into a slotted molybdenum rod. The Mo rod was then inserted into a 3 mm diameter round brass tube which was then filled with copper based epoxy (see Fig. 3a). The Mo-rod and encapsulation help to protect the oxide layer during subsequent mechanical polishing. The sample was polished to a mirror finish with 1200 grit sandpaper followed by 3 μm diamond paste on Vel-Cloth, 1 μm diamond paste on White-Cloth and a final polish with a 0.05 μm colloidal silica solution.

A schematic drawing of the thick sample final design is shown in Fig. 3b. The thickness of the samples in the transverse direction is approximately 200 μm. The incident beam being parallel to the transverse direction, the detected XANES signal as a function of oxide depth is a combination of contribution from the alloying element (Fe or Nb) in precipitates and in solid solution. Because, the X-ray attenuation lengths are approximately 12.5 μm at 7.12 keV and 28 μm at 18.98 keV [25], the sampled volume is tens of microns deep and the alloying elements both in solid solution and in precipitates undergo electron fluorescence reactions causing the detected XANES spectra to be a combination of both signals.

For instance, in Zircaloy-4, assuming that:

- The ratio of Fe and Cr in the precipitates and in the alloy is the same, which has been found to be true for Fe(wt%)/Cr(wt%) < 4 [5], so that the Fe weight concentration in a $Zr(Fe_{0.66}Cr_{0.33})_2$ precipitate, W_{Fe}^{SPP}, is equal to 37.1wt%.

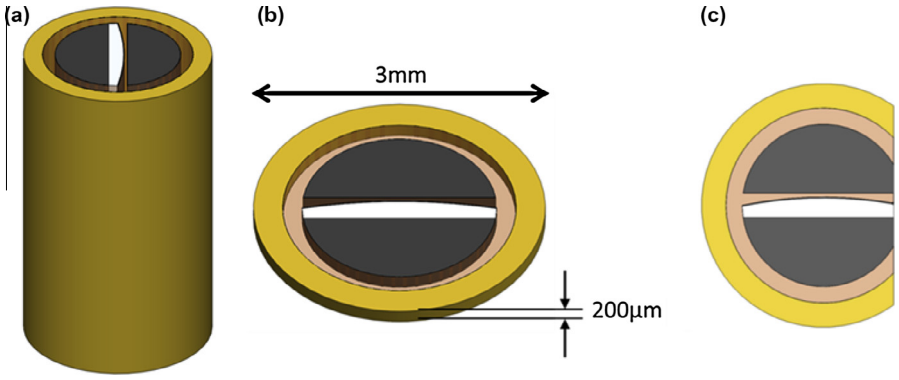

Fig. 3. Thick sample preparation for XANES experiments: (a) sample tubing, (b) final thick sample preparation after cutting and polishing and (c) thin sample preparation after the cut. The brass tube is in yellow, the Mo rod in gray, the epoxy in pink, and the sample in white. The oxide is attached on the surface of the rounded side of the cross-section. (For interpretation of the references to colour in this figure legend, the reader is referred to the web version of this article.)

- The weight concentration of Fe in solid solution, W_{Fe}^{matrix}, is between 50 and 300 wt ppm [4,26–28] and the total amount of Fe in the alloy is equal to 2000 wt ppm.
- The precipitate volume fraction V_F^{SPP} is approximately 0.5%.

Thus the amount of Fe in second phase precipitates is given by $W_{Fe}^{SPP}/W_{Fe}^{matrix} \times V_F^{SPP}$ or five to forty times the amount of Fe in solid solution. Although the Fe fluorescence signal is not directly proportional to the amount of Fe, we can conclude that the contribution of alloying elements in solid solution in the XANES signal coming out from the bulk samples cannot be totally neglected.

2.2.2. Thin sample preparation

To be able to separate the two contributions, a thin cross-sectional sample was prepared from a pre-transition Zircaloy-4 sample (oxide thickness equal to ~1.7 μm). Dimpling or ion milling methods could not be used because they could damage the oxide layer and result in inhomogeneous sample thickness, which is known to alter the XANES signal [29].

The preparation of a cross-sectional thin sample involved a few extra steps from the thick sample one. Once the final thick sample cross-section configuration has been obtained, as described in the previous section, one side of the brass tube was cut using a low speed diamond saw to expose the oxide azimuthal cross section (the azimuthal direction being normal to the azimuthal cross section, see Fig. 3c). Using focused ion beam (FIB) deposition on the rolling cross section (perpendicular to the cut), tungsten was deposited on the form of a small rectangle (75 μm × 20 μm × 10 μm) covering the metal, the oxide and the epoxy (see Fig. 4a). This deposition is necessary to homogenize the ion milling rate of the different phases (metal, oxide and epoxy) and to protect the area that is going to be analyzed at the synchrotron from significant ion damage. Then, using FIB, we ion milled the rolling cross section with silicon atoms using a 20 nA current (see Fig. 4b). Once enough material has been removed, the wedge is polished with FIB at a ±7° angle to obtain a sharp wedge by successively reducing the ion beam current up to 1 nA (see Fig. 4c). A schematic of the polished area is shown in Fig. 5.

This sample preparation also allows us to keep the same data acquisition geometry. The synchrotron X-ray beam is still perpendicular to the sample surface, parallel to the transverse direction. The polished oxide cross section was approximately 30 μm long. Using the detected transmitted signal and the characteristic attenuation length of ZrO_2, the FIB'd sample thickness has been determined to be approximately equal to 12 μm.

To determine whether this sample thickness is small enough to identify areas in the oxide where no precipitates are present, it is necessary to compute the theoretical probability of hitting a precipitate as a function of the sample thickness. We use for this a derivation previously performed in [4]. A scheme of the geometry used in this derivation is shown in Fig. 6. Neglecting the secondary fluorescence, the probability to hit a single precipitate is given by:

$$P = 1 - e^{-N_{SPP}\left(\frac{\pi}{2\sin(\psi_0)}d(r_B+r_{SPP})^2\right)} \quad (1)$$

where N_{SPP} is the precipitate density in cm^{-3}, d is the sample thickness in cm, r_B and r_{SPP} are respectively the synchrotron X-ray beam radius and the precipitate radius and ψ_0 is the synchrotron X-ray incident beam angle. TEM examinations of SPP in Zircaloy-4 have been performed on electropolished samples to estimate r_{SPP} and are shown in Fig. 7. Combining TEM results and beamline characteristics, the following parameters are obtained: $N_{SPP} = 10^{12}\ cm^{-3}$, $r_B = 100$ nm, $r_{SPP} = 100$ nm and $\psi_0 = 90°$. Using these values, the probability to hit a precipitate (solid line) and the calculated transmitted intensity ratio (dashed line) as a function of oxide depth in ZrO_2 are shown in Fig. 8. In the case of the thick sample (~200 μm), the probability of hitting one precipitate is 100% and thus deconvolution of Fe signals is impossible. The probability of hitting a precipitate with a sample thickness of 10–15 μm ranges between 70% and 90%. This is, however, for a "blind" spot. If one obtains a compositional map before acquisition and positions the beam in a low concentration region, the probability to avoid hitting a precipitate is much lower. It is thus theoretically possible to find volumes in the oxide layer where no precipitates will be hit by the incident beam and where the Fe K-edge XANES signal will only come from Fe in solid solution. In conclusion, the thin sample theoretically fulfills the purpose detailed at the beginning of this section.

2.3. Standards

In order to determine the chemical state of Fe and Nb in the zirconium oxide layer, the Fe and Nb K-edge XANES spectra of reference standards were measured. In this study, the XANES spectra of standards were acquired in fluorescence mode. A total of seven standards were used for Fe in Zircaloy-4 (4 metal standards and 3 oxide standards), six standards for Fe in ZIRLO (3 metal and 3 oxide) and five standards for Nb in Zr–2.5Nb and ZIRLO (2 metal and 3 oxide). The list of standards and their origins are shown in Table 2.

The XANES spectra are processed using the Athena software (version 0.8.061, Ifeffit 1.2.11c) [30]. After defining a pre-edge line, the edge energy (highest edge inflection point) and a post edge line to determine the edge step, the spectrum is normalized. The

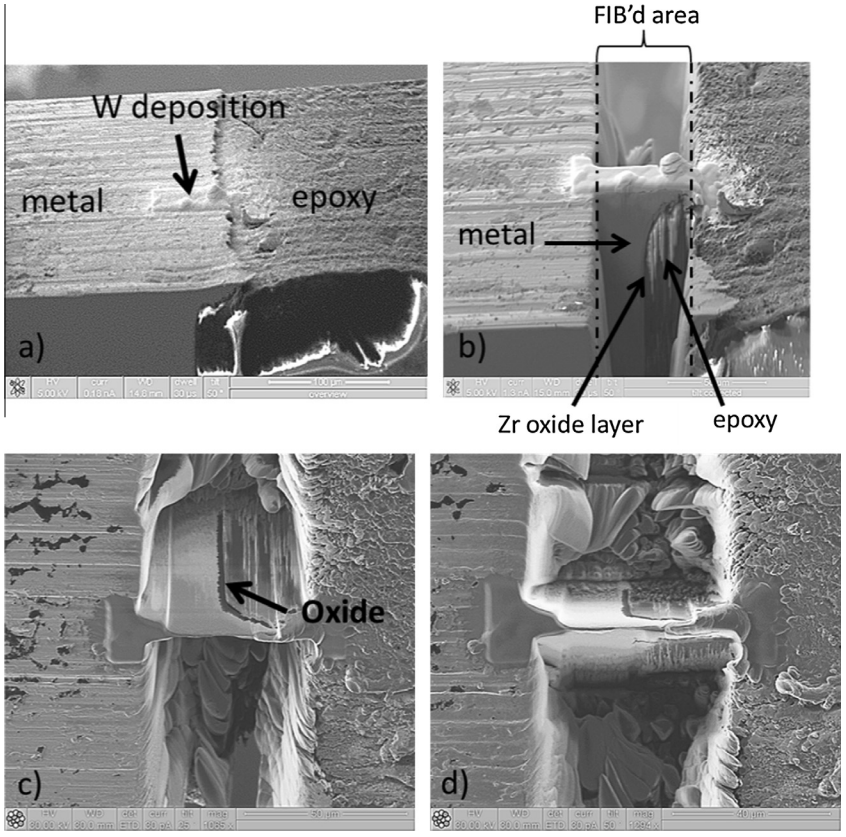

Fig. 4. Secondary electron micrograph of the rolling cross section of the thin sample: (a) tungsten deposition across the interface, (b) ion milling around the deposition, (c) focused ion beam milling of the wedge to reveal the oxide layer with a tilt of ±10° along the normal axis.

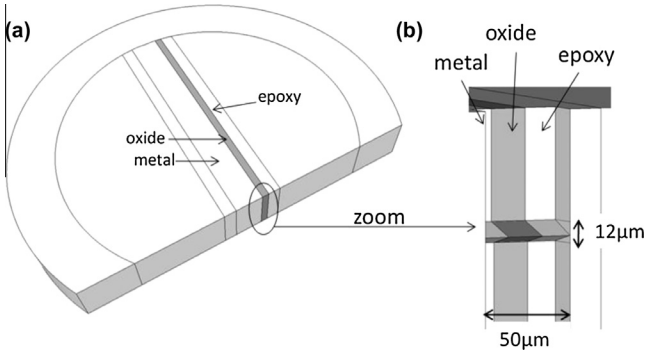

Fig. 5. (a) 3D Schematic drawing of the thin sample and (b) zoom on the thin part of the sample after FIB milling.

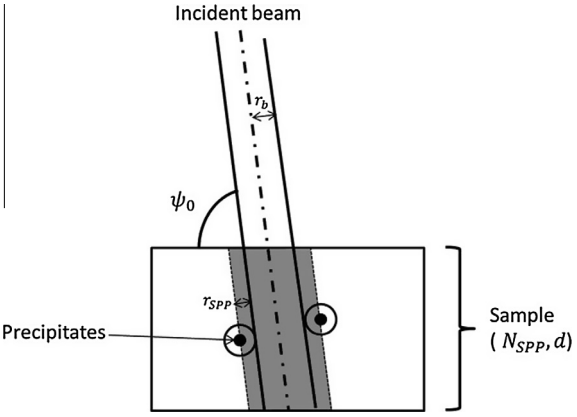

Fig. 6. Schematic drawing of the geometry used to determine the probability to hit a single precipitate.

normalization constant is evaluated by extrapolating the pre- and post-edge lines to the edge energy and subtracting the edge energy-crossing of the pre-edge line from the edge energy-crossing of the post-edge line. This difference is the value of the edge step parameter used in the normalization algorithm. Then the post edge is flattened using Athena's flattening algorithm.

2.3.1. Fe in Zircaloy-4 and in ZIRLO

In the case of Fe, we used bcc-Fe, FeO, Fe_3O_4, and Fe_2O_3 powders obtained from Alfa Aesar as reference spectra. To simulate the various concentrations of Fe in Zircaloy-4, the Fe powders were mixed with a monoclinic ZrO_2 powder at weight fraction levels of 100%, 10%, 1%, 0.1% and 0.01% of Fe in ZrO_2.

However, it is known that metallic Fe in Zircaloy-4 precipitates exhibit a Laves phase crystal structure $Zr(Fe,Cr)_2$ [5,31]. To serve as metallic standard for Fe in the alloy, we measured a Fe XANES spectrum in the metal part of Zircaloy-4 thick sample (designated type #1).

To acquire the standard spectra of metallic Fe in Laves crystal structure $Zr(Fe,Cr)_2$, we also used the thin sample previously described and located a precipitate in the metal part. A 2D Fe fluorescence map of the metal part is presented in Fig. 9, in which the location of the precipitate is shown. A XANES spectrum at the precipitate location was acquired (designated type #2) as the closest reference to a pure $Zr(Fe,Cr)_2$ precipitate found in Zircaloy-4.

Finally, another metallic Fe standard was used. A Fe K-edge XANES spectra of a thick pure zirconium sponge sample with an

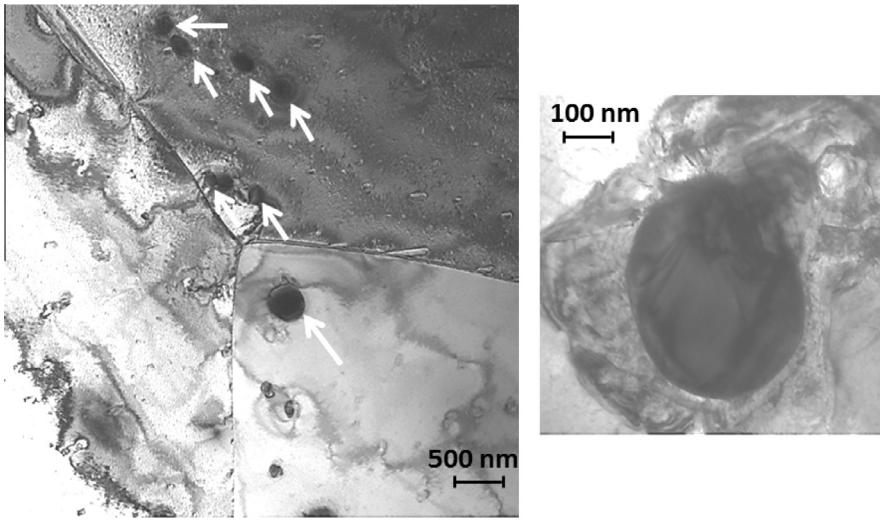

Fig. 7. TEM bright field images of $Zr(Fe,Cr)_2$ precipitates (indicated by arrows) in the metal of Zircaloy-4 sheet alloy (prepared by electropolishing), and expanded view on a $Zr(Fe,Cr)_2$ precipitate (images acquired on a JEOL LaB_6 TEM of 200 keV).

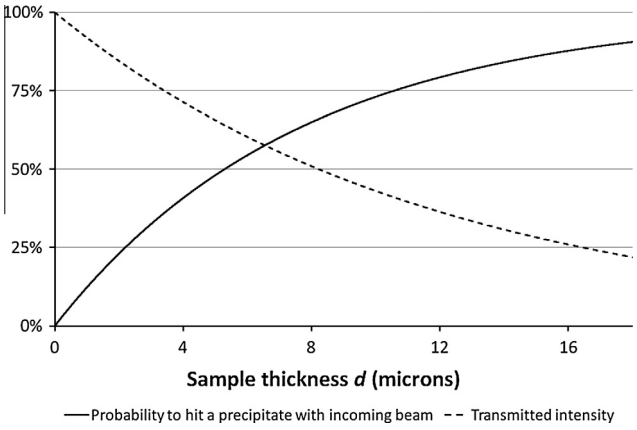

Fig. 8. Probability to hit a single precipitate in a Zircaloy-4 sample with $N_{SPP} = 10^{12}$ cm^{-3}, $r_B = 100$ nm, $r_{SPP} = 100$ nm and $\psi_0 = 90°$ as a function of the sample depth d in micrometers. The theoretical ratio of the transmitted beam intensity over the incident beam intensity in ZrO_2 as a function of the bulk sample depth d is also shown on the same scale.

impurity level of 100–600 wt ppm of Fe has also been acquired (designated type #3) as the closest reference to Fe in solid solution in zirconium.

The XANES spectra of reference standards of metallic Fe in zirconium alloys are presented in Fig. 10a along with the bcc Fe standard, the Fe_2O_3 and Fe_3O_4 spectra. The value of the first inflection point is similar for all the metallic Fe standards (~7.106 keV), which confirms that the chemical state of Fe is metallic. However, the pre-edge and edge features of Fe standards in zirconium are different from those seen in the bcc Fe spectra. The spectra from metallic Fe in Zircaloy-4 (standards #1 and #2) and in pure Zr (#3) show no major differences in the pre-edge and edge features.

Similar spectra were obtained for Fe in ZIRLO. We measured Fe XANES spectrum in the metal part of a ZIRLO thick sample (similar to #1 in Zircaloy-4) to use as metallic standard. However, even though a thin ZIRLO sample was prepared, the precipitates in ZIRLO were too small to be detected individually. Thus a standard of type #2 could not be acquired for ZIRLO.

2.3.2. Nb in ZIRLO and in Zr–2.5Nb

A similar approach was used to acquire XANES spectra of metallic and oxidized Nb standards. In the case of Nb, we used metallic Nb, NbO, NbO_2, and Nb_2O_5 powders as reference spectra. Also, a Nb metallic spectrum has been acquired both in ZIRLO and Zr–2.5Nb metal parts of thick samples to use as metallic standards (similar to #1 for Zircaloy-4).

A summary of all the standards used in this study is shown in Table 2. The XANES spectra of reference standards of metallic Nb are presented in Fig. 10b along with the NbO, NbO_2 and Nb_2O_5 spectra.

Table 2
List of the different standards used in the fitting process of XANES spectra.

	Alloy	Metal standards	Oxide standards
Fe	Zircaloy-4 and Zr–0.4Fe–0.2Cr	Fe bcc	Fe_2O_3 powder
		Fe in Zircaloy-4 metal (#1)	Fe_3O_4 powder
		Fe in $Zr(Fe,Cr)_2$ SPP (#2)	FeO powder
		Fe in pure Zr (#3)	
	ZIRLO	Fe bcc	Fe_2O_3 powder
		Fe in ZIRLO metal (#1)	Fe_3O_4 powder
		Fe in pure Zr (#3)	FeO powder
Nb	ZIRLO	Nb powder	NbO powder
		Nb in ZIRLO metal (#1)	NbO_2 powder
			Nb_2O_5 powder
	Zr–2.5Nb	Nb powder	NbO powder
		Nb in Zr–2.5Nb metal (#1)	NbO_2 powder
			Nb_2O_5 powder

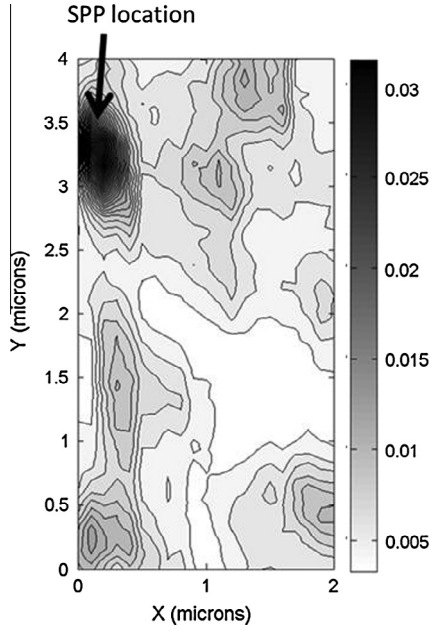

Fig. 9. Fe fluorescence 2D map of a metallic region in the thin Zircaloy-4 sample. The SPP location is indicated by an arrow. The gray scale indicates the normalized number of Fe fluorescence counts per seconds.

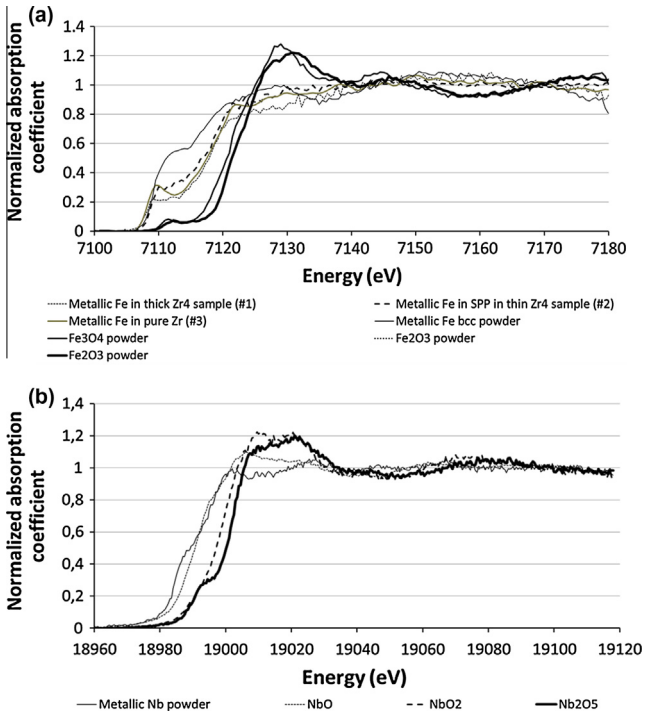

Fig. 10. (a) Normalized fluorescence (in counts/s) of Fe K-edge XANES spectra of powder standards with different Fe chemical states, (b) normalized fluorescence (in counts/s) of Nb K-edge XANES spectra of powder standards with different Nb chemical states.

3. Results

3.1. Thin Zircaloy-4 sample

A 11 μm × 11 μm Fe fluorescence 2D map of the thin Zircaloy-4 sample was acquired around the oxide/metal interface on the ion polished cross section using a step size of a 100 nm. The ratio of the transmitted beam intensity to the incident beam intensity was approximately equal to 35%, which confirmed that the sample thickness was approximately 12 μm.

Using the Fe fluorescence 2D map, three different "lines" along the oxide depth were selected: one in which no detectable precipitates were present ((1) in Fig. 11) and two in which precipitates were present in the oxide (the Cr fluorescence signal corroborates the presence of the precipitates) named SPP1 and SPP2 scans ((2) and (3) in Fig. 11). In Fig. 11, the oxide thickness direction is in the Y direction and its position is determined using the Zr fluorescence signal (not shown here). The oxide is located from $Y = 0$ (oxide/metal interface) to approximately $Y = 1.7$ μm (oxide/epoxy interface). The Fe fluorescence signals along the oxide depth for these three scans are presented in Fig. 12. The FWHM fluorescence peak associated with Fe signal from the precipitates are approximately equal to 0.6 μm and thus are 3 times bigger than the average precipitate size. This is caused by the Gaussian shape of the X-ray beam. Indeed, when the tails of the Gaussian beam hit a precipitate, the fluorescence signal significantly increases due to much higher Fe concentration in precipitates. The two precipitates have approximately the same sizes (as defined by the FWHM) and are fully embedded in the oxide layer. The small increase in Fe fluorescence at the oxide/water interface is due to the Fe pollution from Fe in the autoclave during the corrosion testing as reported previously [32]. XANES spectra have been acquired along those three lines. Fig. 13 shows the XANES spectra for several depths acquired along the scan (1). It is clear that the pre-edge and edge features evolve and consequently, the chemical state of Fe varies along the oxide depth. To quantify the Fe chemical state evolution we used the linear combination fitting algorithm of Athena in which an unknown spectrum is fitted by a linear combination of standard spectra as explained in Section 2. In all cases, the whole spectrum was fitted (pre-edge, edge and post-edge). The standards shown in Table 2 were used in the linear combination fitting process. The unknown spectra is fitted using a linear combination of standards, so that the combinatorial fit has the following mathematical form:

$$\text{fit} = \sum_i a_i S_i \tag{2}$$

where a_i is the weight (or fraction) associated to the ith standard S_i. The fitting was not sensitive enough to detect the differences between FeO, Fe_3O_4 and Fe_2O_3 oxide standards, so the fractions a_i attributed to the oxide reference samples (FeO, Fe_3O_4 and Fe_2O_3 powders) were summed as one overall oxide fraction a_{ox}. The same was done with the metallic Fe standards, which was represented by one Fe metallic fraction a_{met}. The linear combination fitting results for the three scans are presented in Fig. 14, where the fraction of oxidized Fe is plotted as a function of oxide depth, when applying the fits to the data shown in Fig. 14. It is clear that oxidation evolves in the oxide layer.

It was possible to separate out the bcc Fe contribution from that of the three metallic Fe in Zr. An example of one of the fits is shown in Fig. 15a where the Fe oxide fraction and Fe metallic fraction given by the fit are also plotted. The fit reproduces well the measured values. The least-square errors for the fits were smaller than 0.2% for all the fits.

As shown in Fig. 14, the fraction of oxidized Fe gradually increases as the beam approaches the oxide/water interface. The oxidation of Fe in solid solution and in precipitates is delayed relative to the Zr oxidation, so that a significant fraction of Fe remains metallic in the oxide layer. It is also clear from Fig. 14 that Fe in the precipitates oxidize less rapidly than the Fe in solid solution since

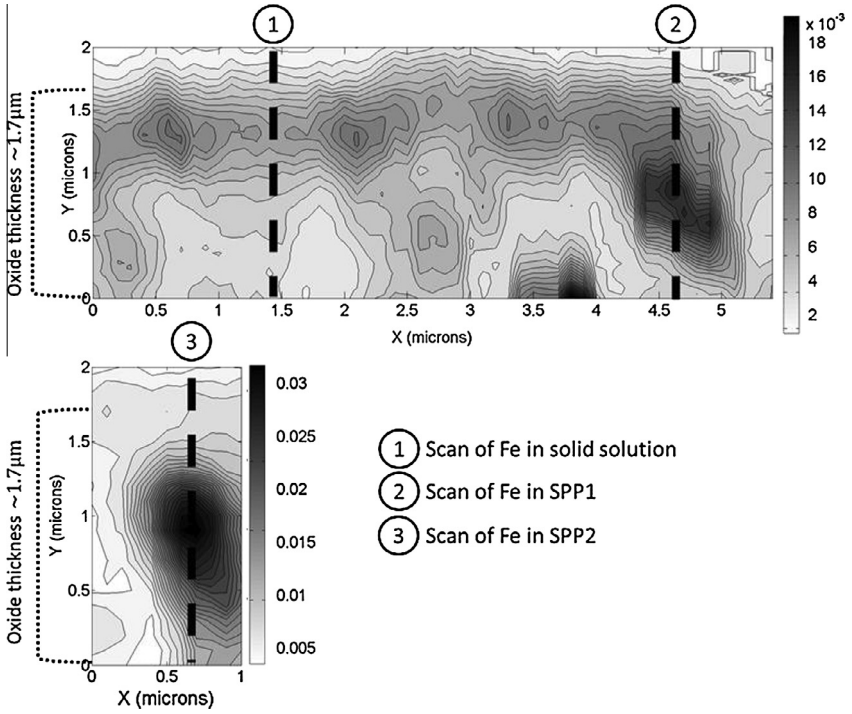

Fig. 11. Fe fluorescence 2D maps of oxide regions in the thin Zircaloy-4 sample showing the lines along which XANES scans (at the Fe K-edge) have been performed. The distance from the oxide/metal interface is represented on the *Y* axis (the oxide/metal interface being at *Y* = 0 has been determined from Zr fluorescence spectra not shown here). The *X* axis is parallel to the oxide/metal interface. The gray scale indicates the normalized number of Fe fluorescence counts (in counts/s).

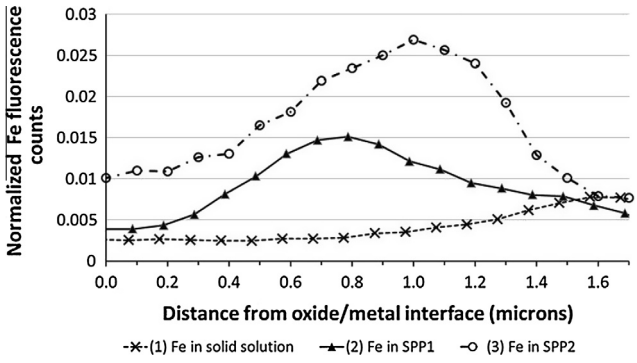

Fig. 12. Scans of normalized Fe fluorescence intensity (in counts/s) of the three different oxide regions in the thin sample.

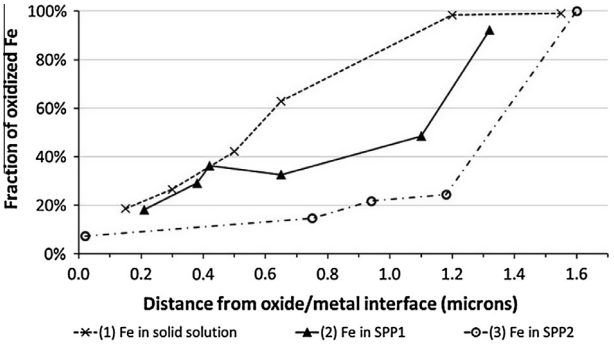

Fig. 14. Fe oxide fraction in the thin Zircaloy-4 sample oxide layer as a function of distance from oxide/metal interface in three different regions (defined in Fig. 11).

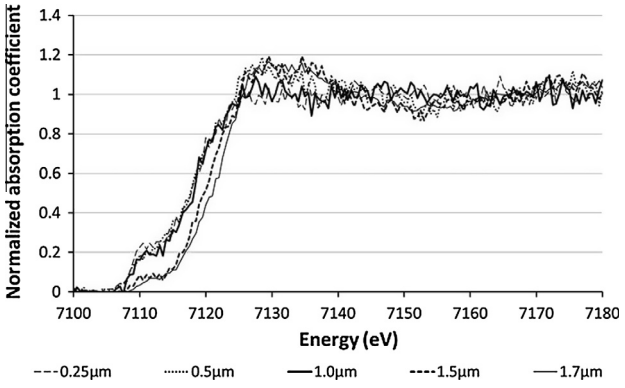

Fig. 13. Normalized fluorescence Fe K-edge XANES spectra at different distances from oxide/metal interface in a thin Zircaloy-4 sample, along a line where no precipitate was detected (see Fig. 11).

for a given depth the fraction of oxidized Fe is higher in the solid solution locations than in the precipitate locations. The precipitates shown in Figs. 11 and 12 are located respectively 0.8 µm (SPP1) away and 1 µm away (SPP2) from the oxide/metal interface. Close to the oxide/metal interface, the beam does not hit the precipitates and the fractions of oxidized Fe in the three regions are similar. As the beam goes further away from the oxide/metal interface, the X-ray beam starts hitting the SPP1 and SPP2 precipitates, the fractions of oxidized Fe of these scans decrease, whereas the fraction of oxidized Fe in solid solution keeps increasing. The lower fractions of oxidized Fe in the SPP1 and SPP2 scans are thus due to the presence of metallic precipitates embedded in the zirconium oxide layer. The fraction of oxidized Fe reaches a minimum where the precipitates are located. As the beam goes away from the precipitate locations toward the oxide/epoxy interface, the fraction of oxidized Fe starts increasing again to reach 100% at the oxide/water interface located approximately at 1.7 µm from the oxide/metal interface for all the scans.

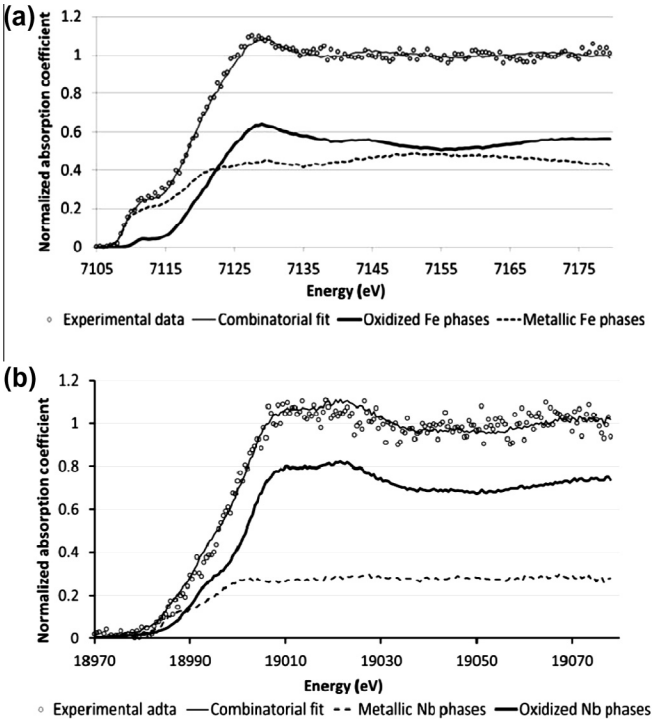

Fig. 15. Linear combination fit of a XANES spectrum in the oxide of a (a) Zircaloy-4 sample, (b) Zr–2.5Nb sample.

3.2. Thick samples

The same data analysis method used on the thin sample was systematically used to fit the data obtained from the thick samples (a fit in the case of Nb in Zr–2.5Nb oxide is also plotted in Fig. 15b). The best fit given by the list of combinatorial fits was used every time and its R-factor plotted as function of incident beam energy to check the precision of the fit and verify if it was homogeneously distributed across the energy range. In each case the Zr fluorescence signal (straight line without symbols in Fig. 16) was acquired to detect the position of the oxide layer and the two interfaces. Fig. 16 shows an example of a post-transition Zircaloy-4 with a total oxide thickness of approximately 3.6 μm that matches that derived from the weight gain. The fraction of oxidized Fe, and its complementary, the fraction of metallic Fe, is also plotted in Fig. 16. The evolution of the fraction of oxidized Fe in the thick samples was similar to that seen in the thin sample. The fraction of oxidized Fe is close to zero at the oxide/metal interface and gradually increases in the protective oxide (oxide formed since the last transition with its thickness derived from weight gain data), until it reaches 100% in the non-protective oxide (oxide formed up to the previous transition), indicating that all the Fe in the non-protective oxide is oxidized. This is expected since this portion of the oxide is thought to be porous and fully permeable to water. It is observed that the oxidation of Fe in the oxide layer is delayed compared to the zirconium oxidation. ZIRLO and Zr–2.5Nb samples show similar results, Nb and Fe exhibit delayed oxidation in the oxide layer.

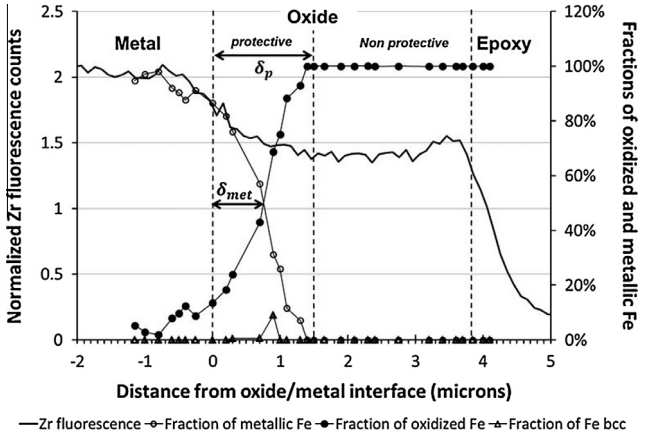

Fig. 16. Fractions of oxidized and metallic Fe along a Zircaloy-4 oxide, as a function of distance from oxide/metal interface. The bcc-Fe fraction is also shown.

The Fe bcc fraction detected in Zircaloy-4 is also plotted in Fig. 16. While it is almost always equal to zero throughout the scan, a measurable Fe bcc signal was normally detected near the region where the precipitates start to oxidize. This result is present in most of the Zircaloy-4 samples that have been investigated in this study, and it is in agreement with previous TEM experiments on Zircaloy-4 samples, which show that a segregation of Fe bcc occurs when the precipitates start oxidizing and the Cr and Zr in the precipitate oxidizing preferentially leaving the Fe to cluster as bcc Fe [17]. The detection of the Fe bcc by this XANES study gives more confidence in the results of the combinatorial fitting as well.

To compare the evolution of alloying element oxidation state between samples of different oxide thickness (i.e. at different exposure time), it is necessary to define a parameter to characterize it and that can be easily evaluated for different samples of the same alloy. The parameter chosen is δ_{met}, the length of the oxide layer in which the fraction of oxidized Fe or Nb is below 50%. Thus δ_{met} is an indication on the evolution of the oxygen potential in the oxide layer. We also define δ_p as the protective oxide thickness (defined as the oxide formed since the previous transition). The ratio δ_{met}/δ_p is an indicator of the fraction of the protective oxide in which alloying elements are mainly metallic. Values of δ_{met} for Fe in Zircaloy-4, ZIRLO and Zr–0.4Fe–0.2Cr and for Nb in ZIRLO and Zr–2.5Nb are shown in Fig. 17. In these plots, δ_{met} is plotted as function of δ_p. It is recalled that δ_p is the portion of the oxide layer formed after the previous transition. The transition thickness is represented by the shaded area. Several transition regimes being analyzed for Zircaloy-4 and ZIRLO the transition is not represented by a straight line, but by a range of thicknesses (the transition thickness is not exactly the same from a transition to another). Small oxide thicknesses have only been investigated in the case of Zircaloy-4, as it is difficult to archive a sample right after its transition. However a general trend of δ_{met} as function of δ_p for Zircaloy-4 and ZIRLO can be observed. At first, δ_{met} increases up to a threshold value of approximately 0.75–0.8 μm for Zircaloy-4 and 1 μm for ZIRLO. During this increase it is important to notice that the ratio δ_{met}/δ_p appears to be approximately constant. Once δ_{met} reaches its threshold value, it remains constant up to when the oxide reaches transition thickness. At the transition (~2.1 μm for Zircaloy-4, ~3 μm for ZIRLO), δ_{met} suddenly drops to zero.

This picture might be slightly different for Zr–2.5Nb and Zr–0.4Fe–0.2Cr alloys. The threshold δ_{met} value for Zr–2.5Nb is at least 1.2 μm and it is at least 1.25 μm for the model alloy Zr–0.4Fe–0.2Cr. But δ_{met} smoothly decreases until the oxide reaches transition and would not remain constant and drop suddenly at transition as it is observed in Zircaloy-4 and ZIRLO alloys. In the case of the model alloy Zr–0.4Fe–0.2Cr, even though the weight gain curve in Fig. 2 does not show transition, the fact that δ_{met} is already dropping significantly for the sample archived at 463 days, suggests that in the future it may undergo transition.

The different transition regimes are indicated for Zircaloy-4 in Fig. 17 and it appears that δ_{met} does not depend on the transition regime. This was expected since δ_{met} is directly dependent on the

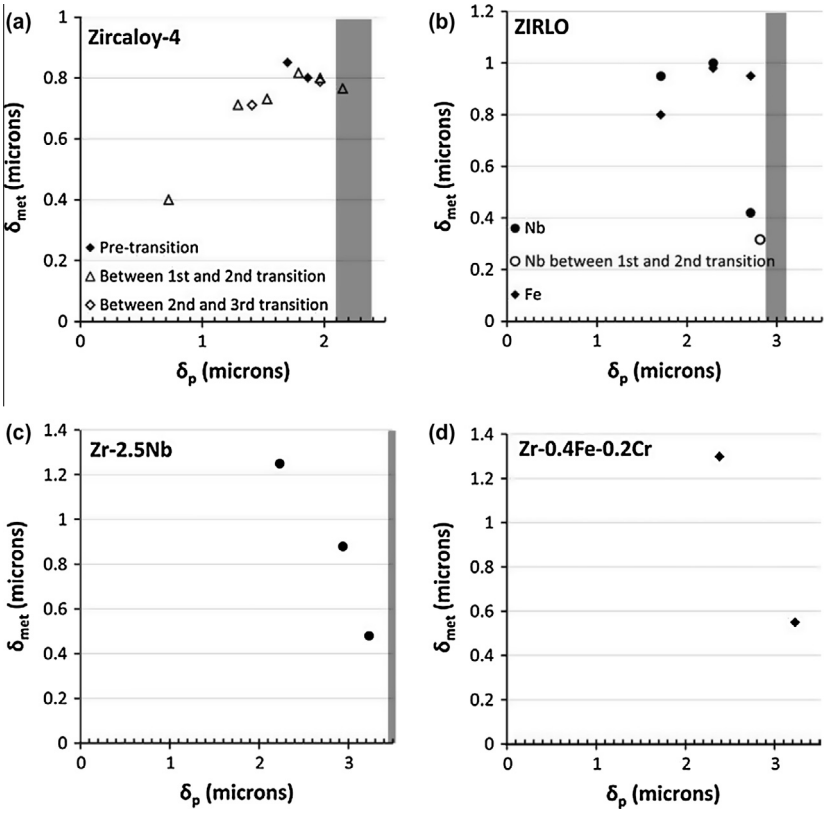

Fig. 17. δ_{met} (in micrometers) as function of the protective oxide thickness δ_p (in micrometers) for: (a) Fe in Zircaloy-4 sheet, (b) Fe and Nb in ZIRLO tube, (c) Nb in Zr–2.5Nb and (d) Fe in Zr–0.4Fe–0.2Cr (H). The shaded area shows transition thickness for the different alloys.

oxygen potential in the oxide layer and it is known that the corrosion of Zircaloy-4 is periodic [32].

The implications of these results are discussed in the following section.

4. Discussion

In Zircaloy-4, ZIRLO, Zr–2.5Nb and Zr–0.4Fe–0.2Cr the oxidation of Fe and Nb in precipitates is delayed relative to Zr oxidation. This is in accordance with previous TEM observations [17,18] and electrochemical measurements [33]. The oxidation of Fe in solid solution in Zircaloy-4 appears to be delayed compared to Zr oxidation according to the results of the thin sample. Thus, Fe in solid solution also remains metallic. One possible mechanism for this to occur is that the Fe "in solid solution" are actually Fe atoms segregated at oxide grain boundaries. Atom probe measurements [34] have shown that this was to some extent the case for Fe in solid solution in the metal part. However we cannot rule out that the observation of Fe in solid solution might be altered by small hidden precipitates undetected in the 2D fluorescence map shown in Fig. 11. In any case, we can conclude that alloying elements in precipitates are protected by the preferential oxidation of zirconium up to a certain distance from the oxide/metal interface where the oxygen potential is high enough to oxidize Fe and/or Nb in precipitates. No bcc Fe signal was detected in the metal (it actually represents 0% of the fit at the oxide/metal interface), and it is only detected when the precipitates embedded in the oxide start oxidizing. It is believed that bcc Fe starts to form when Zr and Cr in the precipitates become oxidized. Indeed Cr has a lower oxidation potential compared to Fe. Once the Cr is oxidized, metallic Fe starts to segregate and forms bcc Fe as observed in [17]. Eventually, once the oxidation potential of Fe in precipitates is reached, Fe starts to oxidize to form Fe_3O_4, and Fe_2O_3 oxides. A similar evolution from Nb metal to Nb oxides also occurs in Nb-based alloys.

An oxidation model based on the μXANES results is proposed:

(1) When a new protective oxide is formed (right after transition), a continuous gradient in oxidation potential in the protective oxide layer is established. The boundary conditions at the oxide/metal and oxide/water (or porous oxide) interfaces fix the oxygen potentials at these locations. As the protective oxide thickens, the oxygen potential gradient decreases but the ratio δ_{met}/δ_p remains constant (even though δ_{met} increases). This situation is schematically described in Fig. 18a (the oxygen potential is represented as the dotted line).
(2) Then δ_{met} reaches a threshold value and remains constant, even though δ_p increases. Thus, the ratio δ_{met}/δ_p decreases and the oxygen potential in the oxide layer cannot remain continuous since the boundary conditions do not change. The oxygen potential in the outer part of the protective oxide increases. This situation is schematically described in Fig. 18b.
(3) Finally, the oxide transition occurs, and δ_{met} is equal to zero (Fe and Nb are fully oxidized). This is because the oxide is no longer protective and is permeable to water. The oxygen potential in the oxide is everywhere higher than the oxidation potential of the alloying elements either in precipitates or in solid solution.

This general oxidation model is valid for Zircaloy-4, ZIRLO and Zr–2.5Nb alloys as well as for the model alloy Zr–0.4Fe–0.2Cr. However, step 2 is dependent on the alloy. Whereas in ZIRLO and

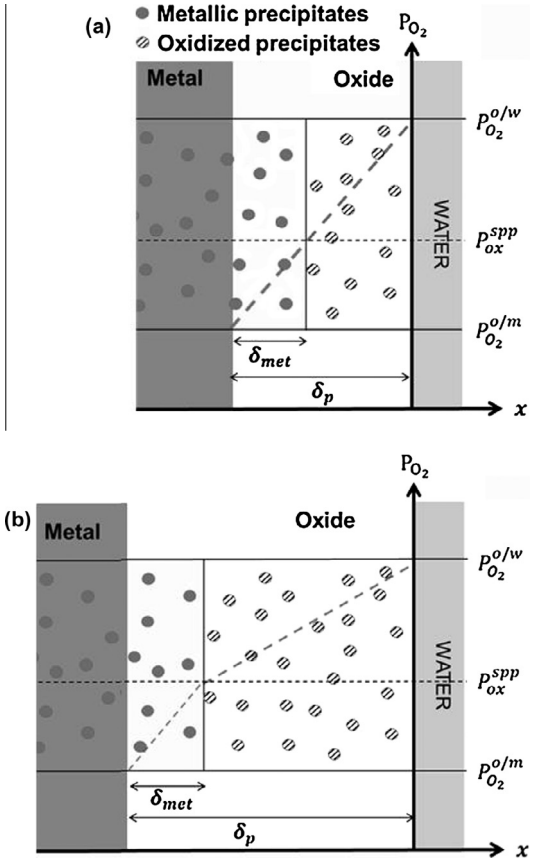

Fig. 18. Schematic evolution of the oxidation of precipitates in zirconium oxide layer as function of the oxygen partial pressure across the oxide: (a) before δ_{met} reached its threshold value, (b) after δ_{met} reached its threshold value.

Zircaloy-4 δ_{met} remains constant until transition and drops to zero just before transition, in Zr–2.5Nb and Zr–0.4Fe–0.2Cr δ_{met} smoothly decreases until transition.

According to the results, a layer, in which most of the alloying elements are metallic, develops as the oxide grows and remains at a constant thickness once the protective oxide reaches a thickness of approximately 1.2–1.5 μm. This threshold thickness is alloy dependent. The threshold value of δ_{met} is smaller in the case of Zircaloy-4 (~750 nm) compared to ZIRLO (~1.0 μm) which is itself smaller than δ_{met} in Zr–2.5Nb and Zr–0.4Fe–0.2Cr alloy (at least 1.2 μm). Sakamoto et al. have found similar results in Zr–2.5Nb alloy with δ_{met} equals to 1 μm for δ_p equals to 1.6 μm [21].

Since δ_{met} is dependent on the element considered, one cannot directly use this parameter to compare the oxidation potential at a given oxide depth between different alloys. However, there is no apparent reason to consider different boundary conditions between the alloys and from free energy calculations the oxidation potential of $Zr(Cr,Fe)_2$ precipitates is higher than the oxidation potential of βNb and on the same order of magnitude than $Zr(Nb,Fe)_2$ precipitates [35]. Thus, at a given location, the oxygen partial pressure in the Zr–2.5Nb oxide layer would be lower compared to the oxygen partial pressure in ZIRLO which would be itself lower than the oxygen partial pressure in Zircaloy-4 oxide layers.

TEM examinations of oxide layers were done on the samples investigated previously by microbeam XANES mainly to locate and confirm the presence of metallic Fe and Nb in precipitates embedded in the oxide layer and finally confront the results with the XANES experiments. The TEM samples were prepared by lift-out technique using FIB with the details of the technique described in length in [36]. This technique produces electron transparent samples with an area of about 10–15 μm in length and 5–10 μm in width of specific regions in the oxide layer. This sample preparation's method was used to be able to study specific areas of the oxide layer, such as precipitates embedded in the oxide. The TEM used was a JEOL LaB_6 TEM of 200 keV.

Diffraction patterns of precipitates embedded in the oxide layer localized by EFTEM and tilting were taken to determine their crystal structure and thus if they were oxidized or not. Some TEM micrographs taken in bright field configuration of a Zircaloy-4 oxide layer ($\delta_p \sim 1.8$ μm) are shown in Fig. 19. The circled precipitates in Fig. 19 are metallic $Zr(Cr,Fe)_2$ precipitates (confirmed by indexing of diffraction pattern). In this specific sample, unoxidized $Zr(Cr,Fe)_2$ precipitates have been observed as far as 400 nm away from the oxide/metal interface, while oxidized ones (appearing as a round/oval shape enclosing small equiaxed ZrO_2 grains separated by many cracks) where seen further than 800 nm away from the oxide/metal interface. Even though the number of investigated precipitates is rather small compared to the statistics of the XANES experiments, these qualitative results are in general agreement with the XANES results as shown in Fig. 17.

Precipitates in ZIRLO oxide scales were also investigated by TEM. However, in that case, rather than the small grained oxides found in Zircaloy-4, the oxidized precipitates would exhibit amorphous contrast as shown in Fig. 20b. Amorphous precipitates show as high oxygen content as the surrounding matrix (as measured by EDS). This might indicate they are oxidized although it is possible that the oxygen signal could also come from the matrix surrounding the investigated precipitates. Thus there is no clear evidence from TEM that amorphous precipitates

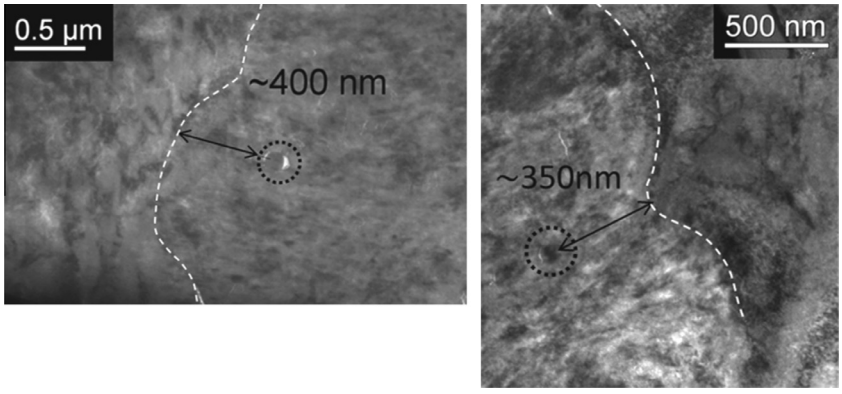

Fig. 19. TEM bright field images of the oxide/metal interface of Zircaloy-4 oxidized for 60 days ($\delta_p \sim 1.8$ μm). Metallic precipitates embedded in the oxide are circled and the oxide/metal interface is also delimited.

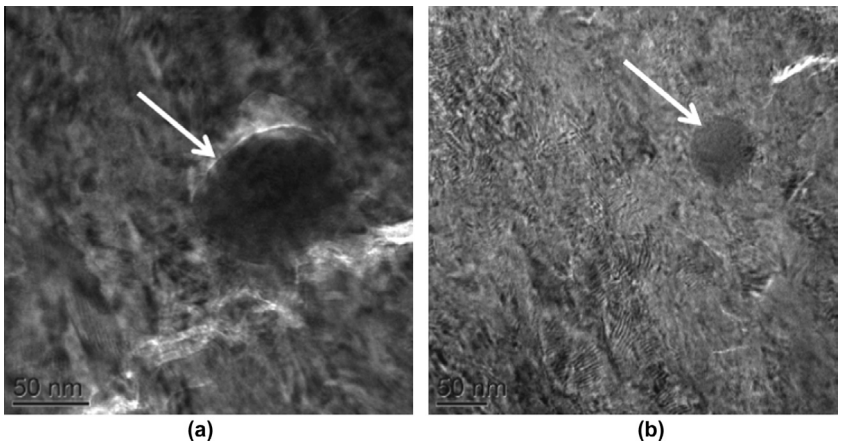

Fig. 20. TEM bright field images of (a) βNb metallic precipitate (250 nm away from the oxide/metal interface), (b) amorphous βNb precipitate (600 nm away from the oxide/metal interface) observed in the oxide layer of a ZIRLO sample oxidized for 120 days ($\delta \sim 3.6$ μm – $\delta_p \sim 0.6$ μm).

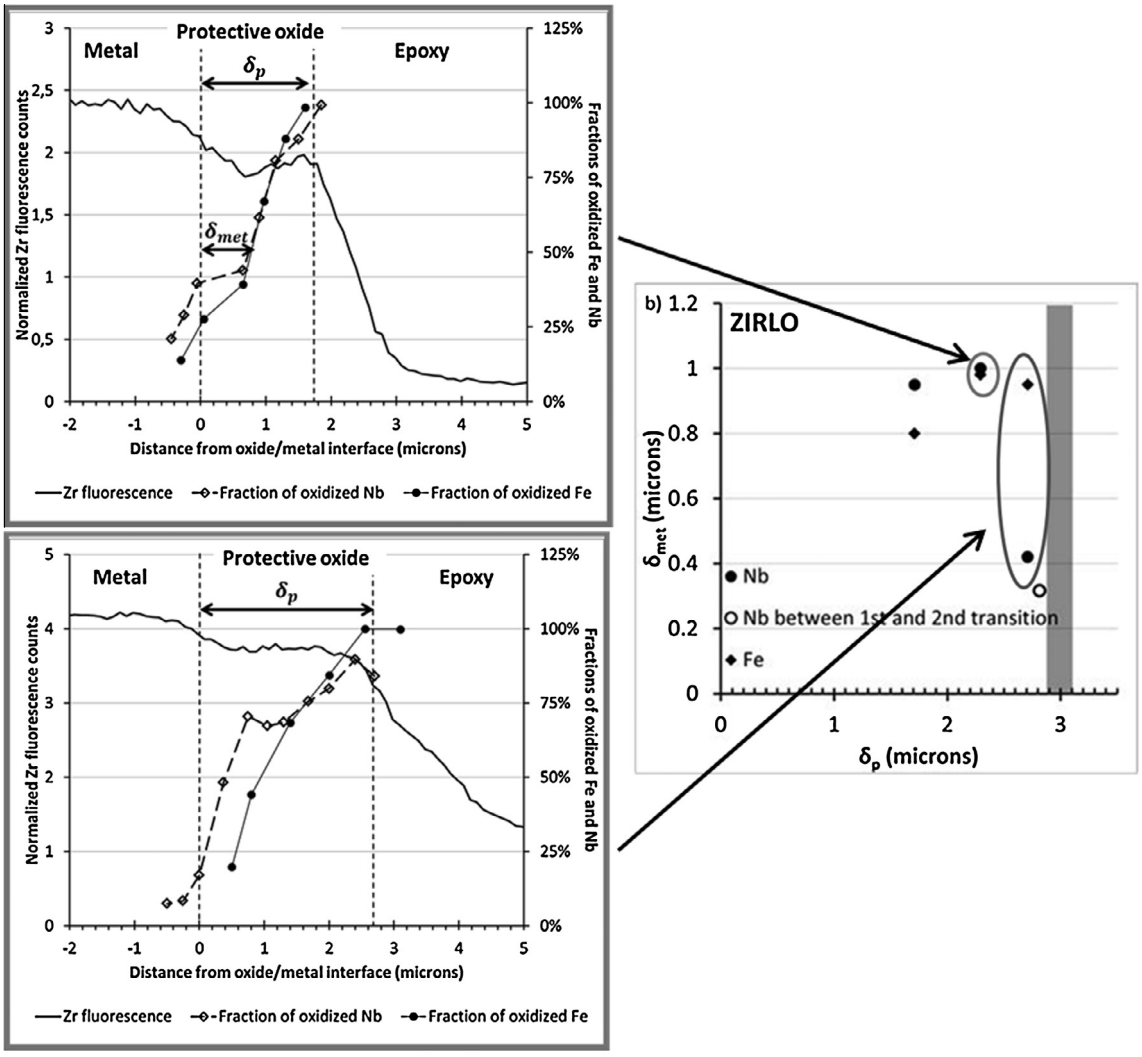

Fig. 21. XANES results on two ZIRLO oxide layers showing the fraction of oxidized Fe and Nb as function of oxide depth. Fig. 17b is plotted on the right to locate the data points corresponding to these analyses.

are actually oxidized in ZIRLO. $Zr(Fe,Nb)_2$ precipitates – that are larger than β-Nb precipitates – remain metallic longer in the oxide: amorphous β-Nb precipitates have been observed as close as 350 nm from the oxide/metal interface (see Fig. 20a), while the closest amorphous $Zr(Fe,Nb)_2$ precipitate was 700 nm away from it for and total oxide thickness of 3.6 μm ($\delta_p \sim 0.6$ μm). Once again these results are in general agreement with the XANES results in Fig. 17.

The development of porosity in these oxide layers could explain why δ_{met} reaches a threshold and why this threshold would be different from alloy to alloy. Many studies have shown a development of porosity in the protective oxide of zirconium alloys [37–41]. However, few of these studies have reported a quantitative analysis of porosity as function of oxide thickness. The evolution of the micro-porosity in zirconium oxide layers as function of oxide thickness has been studied by Ni et al., using TEM Fresnel contrast to localize small pores (1–3 nm) in the oxide layer [42]. The distance from the oxide/metal interface up to where the pores start to be vertically connected in the oxide has been measured for different alloys. For a Zircaloy-4 sample with δ_p = 1.5 μm (pre-transition), this distance was approximately equal to 600 nm. For a second Zircaloy-4 sample with δ_p = 1.9 μm (still pre-transition) this distance increased to approximately 1 μm. For a post-transition ZIRLO sample ($\delta_p \sim 1$ μm), a distance of 700 nm was measured. These values of an oxide thickness free of inter-connected pores are in very good agreement with our reported values of δ_{met} as a function of δ_p (see Fig. 17), from the XANES experiments and also with the reported distances from the oxide/metal interface where metallic precipitates are found with TEM. The formation of a connected network of pores would be related to the oxidation of precipitates, suggesting that the inter-connection of pores would increase the mobility of the oxidizing species (such as oxygen anions) and increasing the partial pressure of oxygen in this part of the oxide layer (see Fig. 18b), which could in turn cause precipitate oxidation. This effect of pores on the mobility of oxidizing species was actually proposed by Cox [3]. However it is unclear if the pores are filled with water and, if so, how does the soaking evolve as the micro-porosity develops. EIS measurements tend to show that liquid soaking of cracks and pores in the protective layer occurs progressively during corrosion [43]. Also, water-filled cracks and pores are in accordance with boron and lithium concentrations variations as function of oxide depths measured by secondary ion mass spectroscopy [44]. In any case, μXANES measurements would agree with an increase in oxygen partial pressure in the outer protective oxide layer due to interconnected porosity development, resulting in a threshold distance from the oxide/metal interface where second phase precipitates remain metallic.

From the same TEM study [42], it was concluded that the oxide porosity increases with the increasing corrosion rate. Yilmazbayhan et al. have shown that for the exact same alloys we are using in this study, the higher the corrosion rate the smaller the oxide thickness at transition [32]. The Zircaloy-4 transition being the earliest (and its corrosion rate the highest), its level of porosity at a given oxide thickness would then be the highest among the considered alloys. This would explain why the value of δ_{met} is smaller in the case of Zircaloy-4 and higher for Zr–2.5Nb. Similarly, the model alloy Zr–0.4Fe–0.2Cr being the most protective of all the alloys (see Fig. 2), it would have the lowest level of porosity in the oxide layer and thus the highest δ_{met} thickness (at least 1.25 μm for this alloy).

The microbeam XANES results on two ZIRLO oxide layers are shown in Fig. 21 for both Fe and Nb. One can notice that δ_{met} at a given δ_p (and so at a given level of porosity) for Fe and for Nb are close to each other. These results would suggest that the oxidation of Fe and Nb in $Zr(Nb,Fe)_2$ occurs simultaneously. But closer to transition Nb is preferentially oxidized compared to the Fe suggesting at least that βNb precipitates oxidize preferentially over $Zr(Nb,Fe)_2$ precipitates. The oxidation free energy of different compounds found in zirconium alloys is available in [35] and the preferential oxidation of βNb precipitates over $Zr(Nb,Fe)_2$ precipitates is confirmed from thermodynamics. However since the βNb precipitates are also smaller than $Zr(Nb,Fe)_2$ precipitates this preferential oxidation of βNb precipitates could also be a kinetic effect (i.e. smaller precipitates are oxidized faster).

According to these results it appears that a sublayer within the oxide, within which alloying elements are mostly metallic, is formed and grows until it reaches a constant thickness due to the formation of interconnected porosity at the outer part of the oxide. This layer in which precipitates are mostly metallic would have a high electronic conductivity compared to the outer layer in which inter-connected pores start to develop and where precipitates are oxidized. Measurements on various zirconium alloys show that the hydrogen pickup has an inverse relationship to the oxide electronic conductivity through the protective oxide of thickness δ_p [23]. Thus, the oxidation of alloying elements either in precipitates or in solid solution would impact the hydrogen pickup. Indeed the evolution of δ_{met} as function of δ_p appears to be correlated to the evolution of the instantaneous hydrogen pickup fraction for a given alloy [45].

5. Conclusions

The oxidation of Fe and Nb alloying elements in second phase precipitates and in solid solution was studied using μXANES in Zircaloy-4, ZIRLO, Zr–2.5Nb and a model alloy Zr–0.4Fe–0.2Cr. The micro-beam resolution allowed us to precisely characterize the oxidation of alloying elements as function of oxide depth. A new type of sample preparation has been developed to probe the oxidation state evolution of Fe in solid solution in Zircaloy-4. These results were also contrasted to TEM examinations.

The results show that:

- Oxidation of Fe and Nb in second phase precipitates are delayed compared to zirconium oxidation. Thus metallic precipitates are embedded into the growing oxide.
- To a lesser extent, oxidation of Fe in solid solution is also delayed compared to zirconium oxidation. This suggests a possible segregation of Fe at oxide grain boundaries.
- An inner layer (of thickness δ_{met}) in which most of the alloying elements in precipitates are still metallic develops as the oxide grows. At first δ_{met} increases as the oxide layer thickens. Then, after the oxide layer thickness reaches an approximate value of 1.2–1.5 μm, δ_{met} remains constant until transition. At transition δ_{met} drops suddenly to zero for ZIRLO and Zircaloy-4 alloys whereas, δ_{met} decreases smoothly to zero for Zr–2.5Nb and Zr–0.4Fe–0.2Cr. These results are confirmed by TEM investigations of precipitates embedded in zirconium oxide layers.
- This threshold δ_{met} value is alloy-dependent and has been connected to the development of micro-porosity in the oxide. It is found that for the various alloys studied, as the corrosion rate increases, the pore density increases, which causes δ_{met} to decrease.
- In addition, TEM examinations of precipitates embedded into the oxide layer have been performed and the results confirm the quantitative analysis of the microbeam XANES measurements.

The evolution of δ_{met}/δ_p is found to correlate with the evolution of the instantaneous hydrogen pickup fraction in all the studied alloys as discussed in another paper [45].

Acknowledgments

The authors would like to thank the Research and Technology Unit of Westinghouse Electric Company for their technical help, and EPRI for financial support. The expertise of Robert Comstock of the Research and Technology Unit of Westinghouse Electric Company has also been greatly valuable to the authors. The authors would also like to thank Kan. Sakamoto from Nippon

Nuclear Fuel Development, Goutam Kuri from Paul Scherrer Institute for helpful discussions and the community of the MUZIC-2 program. Usage of the Advanced Photon Source was supported by the U.S. Department of Energy, Office of Basic Energy Sciences under Contract No. DE-AC02-06CH11357.

References

[1] Corrosion of Zirconium Alloys in Nuclear Power Plants, ed. IAEA-TECDOC-684, Vienna, 1993.
[2] Waterside Corrosion of Zirconium Alloys in Nuclear Power Plants, ed. IAEA-TECDOC-996, Vienna, 1998.
[3] B. Cox, J. Nucl. Mater. 336 (2005) 331–368.
[4] A. Yilmazbayhan, O. Delaire, A.T. Motta, R.C. Birtcher, J.M. Maser, B. Lai, J. Nucl. Mater. 321 (2003) 221–232.
[5] D. Charquet, R. Hahn, E. Ortlieb, J.-P. Gros, J.-F. Wadier, Solubility limits and formation of intermetallic precipitates in ZrSnFeCr alloys, in: Zirconium in the Nuclear Industry: 8th Symposium, ASTM STP 1023, 1988, pp. 405–422.
[6] G.P. Sabol, R.J. Comstock, R.A. Weiner, P. Larouere, R.N. Stanutz, In-reactor corrosion performance of ZIRLO and Zircaloy-4, in: Zirconium in the Nuclear Industry: 10th International Symposium, ASTM STP 1245, Baltimore, 1994, pp. 724–744.
[7] G.P. Sabol, G.R. Kilp, M.G. Balfour, E. Roberts, Development of a cladding alloy for high burnup, in: Zirconium in the Nuclear Industry: 8th International Symposium, ASTM STP 1023, San Diego, 1989, pp. 227–244.
[8] J.P. Abriata, J.C. Bolcich, Bull. Alloy Phase Diagrams 3 (1982) 1710–1712.
[9] K. Kakiuchi, N. Itagaki, T. Furuya, A. Miyazaki, Y. Ishii, S. Suzuki, T. Terai, M. Yamawaki, J. Phys. Chem. Solids 66 (2005) 308–311.
[10] Y. Hatano, R. Hitaka, M. Sugisaki, M. Hayashi, J. Nucl. Mater. 248 (1997) 311–314.
[11] S. Kass, J. Electrochem. Soc. 107 (1960) 594–597.
[12] W.E. Berry, D.A. Vaughan, E.L. White, Corrosion 17 (1961) 109.
[13] H.H. Klepfer, Corrosion 19 (1963) 285.
[14] K.-N. Choo, S.-I. Pyun, Y.-S. Kim, J. Nucl. Mater. 226 (1995) 9–14.
[15] B. Cox, J. Nucl. Mater. 264 (1999) 283–294.
[16] http://www.doitpoms.ac.uk/tlplib/ellingham_diagrams/interactive.php.
[17] D. Pêcheur, F. Lefebvre, A.T. Motta, C. Lemaignan, J.F. Wadier, J. Nucl. Mater. 189 (1992) 318–332.
[18] D. Pêcheur, J. Nucl. Mater. 278 (2000) 195–201.
[19] K. Sakamoto, K. Une, M. Aomi, Chemical state of alloying elements in oxide layer of Zr-based alloys, in: LWR Fuel Performance/Top Fuel/WRFPM, Orlando, FL, 2010.
[20] K. Sakamoto, K. Une, M. Aomi, K. Hashizume, Prog. Nucl. Energy 57 (2012) 101–105.
[21] K. Sakamoto, K. Une, M. Aomi, K. Hashizume, Oxidation behavior of Niobium in oxide layers of zirconium-niobium alloys, in: Top Fuel 2012, Manchester, UK, 2012, pp. 297–306.
[22] A. Froideval, C. Degueldre, C.U. Segre, M.A. Pouchon, D. Grolimund, Corros. Sci. 50 (2008) 1313–1320.
[23] A. Couet, A.T. Motta, R.J. Comstock, J. Nucl. Mater. 451 (2014) 1–13.
[24] Standard Test Method for Corrosion Testing of Products of Zirconium, Hafnium, and Their Alloys in Water at 680°F or in Steam at 750°F, ASTM G2/G2M-06, West Conshohocken, PA Patent, 2011.
[25] B.L. Henke, E.M. Gullikson, J.C. Davis, At. Data Nucl. Data Tables 54 (1993) 181–342.
[26] K. Loucif, P. Merle, R. Borrelly, J. Nucl. Mater. 202 (1993) 193–196.
[27] R. Borrelly, P. Merle, L. Adami, J. Nucl. Mater. 170 (1990) 147–156.
[28] C. Li, B. Zhou, W. Zhou, P. Li, Q. Peng, S. Ying, B. Shen, J. Nucl. Mater. 304 (2002) 134–138.
[29] J. Goulon, C. Goulon-Ginet, R. Cortes, J.M. Dubois, J. Phys. France 43 (1982) 539–548.
[30] http://cars9.uchicago.edu/ifeffit/BruceRavel/Horae.
[31] C. Lemaignan, A.T. Motta, Zirconium Alloys in Nuclear Applications, vol. 10B, B.R.T. Frost, 1994.
[32] A. Yilmazbayhan, A.T. Motta, R.J. Comstock, G.P. Sabol, B. Lai, Z. Cai, J. Nucl. Mater. 324 (2004) 6–22.
[33] P. Barberis, E. Ahlberg, N. Simic, D. Charquet, M. Dahlback, M. Limback, P. Tagstrom, C. Lemaignan, G. Wikmark, B. Lehtinen, Role of second phase particles in binary zirconium alloys, in: Zirconium in the Nuclear Industry: 13th International Symposium, ASTM STP 1423, 2001, pp. 33–58.
[34] D. Hudson, G.D.W. Smith, Scripta Mater. 61 (2009) 411–414.
[35] C. Proff, S. Abolhassani, C. Lemaignan, J. Nucl. Mater. 432 (2013) 222–238.
[36] L.A. Giannuzzi, F.A. Stevie, Micron 30 (1999) 197–204.
[37] P. Bossis, G. Lelievre, P. Barberis, X. Iltis, F. Lefebvre, Multi-scale characterization of the metal-oxide interface of zirconium alloys, in: Zirconium in the Nuclear Industry: Twelfth International Symposium, ASTM STP 1354, 2000, pp. 918–945.
[38] B. Cox, J. Nucl. Mater. 148 (1987) 332–343.
[39] N. Ramasubramanian, P. Billot, S. Yagnik, Hydrogen evolution and pickup during the corrosion of zirconium alloys: a critical evaluation of the solid state and porous oxide electrochemistry, in: Zirconium in the Nuclear Industry: Thirteenth International Symposium, ASTM STP 1423, Philadelphia, USA, 2002, pp. 222–244.
[40] R.A. Ploc, S.B. Newcomb, Porosity in Zr–2.5Nb corrosion films, in: Microscopy of oxidation 3: Proceedings of the Third International Conference on the Microscopy of Oxidation, University of Cambridge, 1996, pp. 475–487.
[41] K. Une, K. Sakamoto, M. Aomi, J. Matsunaga, Y. Etoh, I. Takagi, S. Miyamura, T. Kobayashi, K. Ito, Hydrogen absorption mechanism of zirconium alloys based on characterization of oxide layer, in: Zirconium in the Nuclear Industry: 16th International Symposium, ASTM STP 1529, 2011, pp. 401–432.
[42] N. Ni, S. Lozano-Perez, M.L. Jenkins, C. English, G.D.W. Smith, J.M. Sykes, C.R.M. Grovenor, Scripta Mater. 62 (2010) 564–567.
[43] J. Schefold, D. Lincot, A. Ambard, O. Kerrec, J. Electrochem. Soc. 150 (2003) B451–B461.
[44] D. Pecheur, J. Godlewski, J. Peybernes, L. Fayette, M. Noe, A. Frichet, O. Kerrec, Contribution to the understanding of the effect of the water chemistry on the oxidation kinetics of zircaloy-4 cladding, in: Zirconium in the Nuclear Industry: Twelth International Symposium, ASTM STP 1354, Toronto, 1998, pp. 793–811.
[45] A. Couet, A.T. Motta, R.J. Comstock, Effect of alloying elements on hydrogen pick-up in zirconium alloys, in: 17th International Symposium on Zirconium in the Nuclear Industry, ASTM STP 1543, Hyderabad, India, 2013.